CrossMark

ORIGINAL ARTICLE

Global search for low-thrust transfers to the Moon in the planar circular restricted three-body problem

Kenta Oshima[1] (ORCID) · **Stefano Campagnola[2]** ·
Tomohiro Yanao[1]

Abstract This paper globally searches for low-thrust transfers to the Moon in the planar, circular, restricted, three-body problem. Propellant-mass optimal trajectories are computed with an indirect method, which implements the necessary conditions of optimality based on the Pontryagin principle. We present techniques to reduce the dimension of the set over which the required initial costates are searched. We obtain a wide range of Pareto solutions in terms of time of flight and mass consumption. Using the Tisserand–Poincaré graph, a number of solutions are shown to exploit high-altitude lunar flybys to reduce fuel consumption.

Keywords Low-thrust transfer · Pareto solution · Planar circular restricted three-body problem · High-altitude flyby · Tisserand–Poincaré graph

1 Introduction

Electric propulsion is a key technology for space exploration, as has been demonstrated by the Deep Space 1 (Rayman et al. 2000), DAWN (Russell et al. 2007), SMART-1 (Racca et al. 2002), and HAYABUSA (Kawaguchi et al. 2008) missions. The high fuel efficiency of ion engines enables microsatellite missions, such as PROCYON (Funase et al. 2014) and Lunar IceCube (Folta et al. 2016). However, the design of low-thrust trajectories remains

✉ Kenta Oshima
  kenta-oshima@akane.waseda.jp

  Stefano Campagnola
  stefano.campagnola@ac.jaxa.jp

  Tomohiro Yanao
  yanao@waseda.jp

[1] Department of Applied Mechanics and Aerospace Engineering, Waseda University,
  Tokyo 169-8555, Japan

[2] Department of Space Flight Systems, ISAS/JAXA, Sagamihara, Kanagawa 155-0031, Japan

a challenging task, especially in the Earth–Moon system, where multi-body dynamics is important and solutions include multiple revolutions.

Several studies have presented optimal low-thrust transfers in the Earth–Moon system, starting from Earth orbits and targeting libration point orbits, distant retrograde orbits, and orbits around the Moon (Kluever and Pierson 1995; Betts and Erb 2003; Topputo 2007; Mingotti et al. 2009; Ozimek and Howell 2010; Caillau et al. 2012; Zhang et al. 2015). Although global searches were sometimes performed (Russell 2007; Ohndorf et al. 2009; Abraham et al. 2013), solutions with longer transfer times have not yet been fully explored. Such solutions cannot be easily designed because they require hundreds of revolutions around the Earth, which is computationally costly, and high-altitude lunar flybys (Ross and Lo 2003; Ross and Scheeres 2007; Topputo et al. 2008; Belbruno et al. 2008; Jerg et al. 2009; Grover and Ross 2009; Campagnola and Russell 2010; Lantoine et al. 2011; Campagnola et al. 2014), which require the use of chaotic dynamics in multi-body regimes.

In the present paper, we compute mass-optimal transfers to the Moon in the planar, circular, restricted, three-body problem for a wide range of transfer times and for two representative thrust levels. The optimal control is computed with an indirect method; however, the transversality conditions are not fully enforced, because of the well-known numerical instabilities of bang-bang solutions (Russell 2007). Instead, we perform an extensive search over the set of initial costates and extract the Pareto-front of suboptimal solutions. In the present study, we apply two techniques to reduce the dimension of the search set: assuming an initial tangential thrust and using the similarity to two-body dynamics on the initial orbit around the Earth. Finally, Pareto-front solutions are analyzed using the Tisserand–Poincaré graph, where low-propellant-mass solutions are found to exploit the 2:5 resonance, as reported by Pernicka et al. (1995) and Topputo et al. (2005) for trajectories using impulsive maneuvers.

The remainder of the present paper is organized as follows. Section 2 summarizes the dynamical model, the Tisserand–Poincaré graph, the optimal control problem, and the method in Russell (2007). Section 3 presents methods by which to reduce the dimension of the search set. Finally, Sect. 4 presents the computational results of low-thrust transfers to the Moon.

2 Background

2.1 Dynamics

The planar, circular, restricted, three-body problem (PCR3BP) describes the motion of a massless particle m (a spacecraft) under the gravitational influence of two massive celestial bodies m_1 (Earth) and m_2 (Moon), which are revolving on circular orbits around their barycenter. This simplified model captures the essential dynamics of a spacecraft in the Earth–Moon system assuming the negligible inclination of the spacecraft trajectory.

In the present study, we consider the dynamics of the PCR3BP in the barycentric rotating frame, where m_1 and m_2 are fixed on the x-axis (Szebehely 1967). The equations of motion include thrust and a mass equation, the dimensionless form of which is given as (Russell 2007)

$$\dot{X} = f(X, u, t), \tag{1}$$

$$X := \begin{bmatrix} r \\ v \\ m \end{bmatrix}, \tag{2}$$

Table 1 Physical constants

Parameter	Value	Unit
Mass parameter μ	0.0121506683	–
Earth mass	5.972×10^{24}	kg
Gravitational constant	6.67384×10^{-11}	$m^3\ kg^{-1}\ s^{-2}$
Standard gravity g_0	9.80665	m/s^2
Distance unit	384405	km
Time unit	4.34811305	day
Moon radius R_M	1738	km
Abscissa of $L_1\ x_{L_1}$	0.8369147189	–
Jacobi constant of $L_1\ C_{L_1}$	3.2003449098	–

$$f(X, u, t) := \begin{bmatrix} v, \\ g(r) + h(v) + uT/m, \\ -T/V_e \end{bmatrix}, \tag{3}$$

where t is time, $r:=[x\ y]^T$, $v:=[v_x\ v_y]^T$, and m are the position, velocity, and mass of a spacecraft, u is the thrust direction ($|u| = 1$), T is the thrust magnitude, V_e is the exhaust velocity of an engine, and

$$g(r):= \begin{bmatrix} x - \frac{\mu(x-1+\mu)}{\{(x-1+\mu)^2+y^2\}^{3/2}} - \frac{(1-\mu)(x+\mu)}{\{(x+\mu)^2+y^2\}^{3/2}} \\ y - \frac{\mu y}{\{(x-1+\mu)^2+y^2\}^{3/2}} - \frac{(1-\mu)y}{\{(x+\mu)^2+y^2\}^{3/2}} \end{bmatrix}, \tag{4}$$

$$h(v):= \begin{bmatrix} 2v_y \\ -2v_x \end{bmatrix}. \tag{5}$$

The equations are non-dimensionalized with a length scale factor of m_1–m_2 distance, a time scale factor of (orbital period of m_1 and m_2)/2π, and a unit mass scale factor of $m_1 + m_2$. Table 1 summarizes the physical constants used for the PCR3BP.

Figure 1a shows an example of a low-thrust transfer in the Earth–Moon PCR3BP. During coast arcs, the system given by Eq. (1) preserves the Jacobi constant

$$C = -(v_x^2 + v_y^2) + (x^2 + y^2) + \frac{2(1-\mu)}{\sqrt{(x+\mu)^2 + y^2}} + \frac{2\mu}{\sqrt{(x-1+\mu)^2 + y^2}} + \mu(1-\mu). \tag{6}$$

Figure 1b shows the change in the Jacobi constant in the final part of the transfer. The final value of the Jacobi constant becomes slightly higher than that of L_1, i.e., C_{L_1}, as shown in the magnified inset figure, which indicates that the spacecraft is energetically captured around the Moon (Koon et al. 2011).

2.2 Tisserand–Poincaré graph

The Tisserand–Poincaré (T–P) graph is a powerful tool for analyzing the global space of solutions. The T–P graph is a Poincaré section of the system given by Eq. (1); the section is placed far from m_2, so that the states of a spacecraft are well represented by its osculating orbital elements around m_1. The graph includes level sets of the Tisserand parameter, which approximates the Jacobi constant and is a measure of the spacecraft velocity relative to m_2 (v_∞).
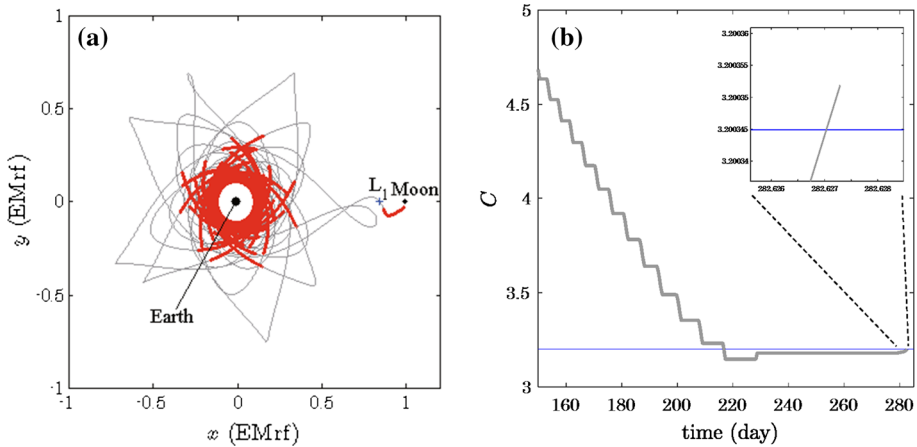
Fig. 1 **a** Example of a low-thrust transfer in the Earth–Moon PCR3BP. The *thick arcs* represent the thrust arcs. **b** Change in the Jacobi constant C in the final part of the transfer in **a**. The *horizontal line* represents the Jacobi constant of L_1. The *inset* figure magnifies the ending part of the change in the Jacobi constant
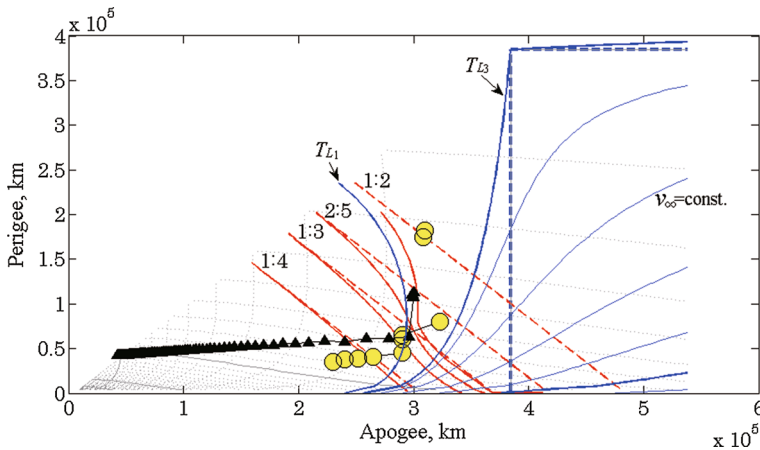
Fig. 2 Osculating perigees and apogees of the trajectory in Fig. 1a (*triangles*) and those of ESA's SMART-1 (*circles*) in the T–P graph

Figure 2 shows an example T–P graph with level sets of the Tisserand parameter. (Here, T_{L_1} is the Tisserand parameter associated with L_1, and T_{L_3} is the Tisserand parameter associated with L_3.) The graph includes lines of slope -1, which are constant-period level sets. The period is determined by the resonant ratio N:M, where N is the number of revolutions of the Moon, and M is the number of spacecraft revolutions in the inertial frame.

Figure 2 also shows the boundaries (solid curves) of the trajectories reachable from the resonances (Campagnola et al. 2012) via a lunar flyby. The region bounded by T_{L_1} and T_{L_3} corresponds to the low-energy regime. There are also the level sets of v_∞ in the patched-conics domain. See Campagnola and Russell (2010) and Campagnola et al. (2012, 2014) for details of the T–P graph.

Figure 2 shows the osculating perigees and apogees of the trajectory in Fig. 1a (triangles) and those of the trajectory of ESA's SMART-1 (circles, for every T–P graph in the present

paper). In order to analyze the trajectories, we plot osculating perigees and apogees on Poincaré sections at perigees only when the distance from the center of the Moon is greater than 70,000 km.

The plot reveals that the trajectory in Fig. 1a exploits the 2:5 resonance before reaching the Moon realm. In the present paper, we demonstrate that this is a common feature of a number of long-time-of-flight solutions. The plot also shows that SMART-1 eventually used the 1:2 resonance. Note that these trajectories move in the low-energy regime, which cannot be handled by the patched-conics model.

2.3 Mass-optimal problem in the PCR3BP

In the present study, we consider mass optimal problems with performance index

$$J = -m_f, \tag{7}$$

and boundary conditions

$$\boldsymbol{\psi}(t_0, t_f, X_0, X_f, \tau) = 0, \tag{8}$$

where the subscripts 0 and f represent initial and final values, respectively, X_0 and X_f are the boundary states of the dynamical system given by Eq. (1), and τ is a parameter, which will be explained more in detail later.

The optimal control Hamiltonian is defined through the costates $\boldsymbol{\lambda}$ as

$$H(X, \boldsymbol{\lambda}, \boldsymbol{u}, t) = \boldsymbol{\lambda}_r^T \boldsymbol{v} + \boldsymbol{\lambda}_v^T (\boldsymbol{g}(\boldsymbol{r}) + \boldsymbol{h}(\boldsymbol{v}) + \boldsymbol{u}T/m) - \lambda_m \frac{T}{V_e}, \tag{9}$$

where the subscripts of $\boldsymbol{\lambda}$ denote the components of $\boldsymbol{\lambda}$.

The Pontryagin principle (Pontryagin 1987) states that the optimal control ($\boldsymbol{u}_{opt}$, T_{opt}) is the one that globally minimizes the Hamiltonian, and is provided by the following equations [see for example Lawden (1963) and Russell (2007)]:

$$\boldsymbol{u} = -\frac{\boldsymbol{\lambda}_v}{|\boldsymbol{\lambda}_v|}, \tag{10}$$

and

$$\begin{aligned} T &= 0 \quad (S < 0), \\ T &= T_{max} \quad (S > 0), \\ 0 &\leq T \leq T_{max} \quad (S = 0), \end{aligned} \tag{11}$$

where

$$S = \frac{|\boldsymbol{\lambda}_v|}{m} + \frac{\lambda_m}{V_e} \tag{12}$$

is the switching function.

The Pontryagin principle also provides the equations of motion for the costates

$$\dot{\boldsymbol{\lambda}}_r = -\left(\frac{\partial \boldsymbol{g}}{\partial \boldsymbol{r}}\right)^T \boldsymbol{\lambda}_v, \tag{13}$$

$$\dot{\boldsymbol{\lambda}}_v = -\boldsymbol{\lambda}_r - \left(\frac{\partial \boldsymbol{h}}{\partial \boldsymbol{v}}\right)^T \boldsymbol{\lambda}_v, \tag{14}$$

$$\dot{\lambda}_m = -|\boldsymbol{\lambda}_v| \frac{T}{m^2}, \tag{15}$$

and the full set of boundary conditions (transversality conditions):

$$H_0 = \frac{d\Phi}{dt_0}, \tag{16}$$

$$H_f = -\frac{d\Phi}{dt_f}, \tag{17}$$

$$\boldsymbol{\lambda}_0 = -\frac{d\Phi}{d\boldsymbol{X}_0}, \tag{18}$$

$$\boldsymbol{\lambda}_f = \frac{d\Phi}{d\boldsymbol{X}_f}, \tag{19}$$

$$0 = \frac{d\Phi}{d\tau}, \tag{20}$$

where

$$\Phi(t_0, t_f, \boldsymbol{X}_0, \boldsymbol{X}_f, \boldsymbol{\nu}) = J + \boldsymbol{\nu}^T \boldsymbol{\psi}(t_0, t_f, \boldsymbol{X}_0, \boldsymbol{X}_f, \tau), \tag{21}$$

and $\boldsymbol{\nu}$ are Lagrange multipliers associated with the boundary constraints given by Eq. (8).

2.4 Brief summary of Russell (2007)

Typical indirect methods try to solve the transversality conditions given by Eqs. (16) through (20), with iterative techniques that rely on first-order derivatives and converge to local minima. They are numerically unstable because of the discontinuous control, which is provided in a feedback form by Eqs. (10) and (11).

For these reasons, Russell (2007) proposed a method of searching through the set of admissible initial states and costates, defined by the initial conditions and by Eqs. (18) and (20), and disregarding the transversality conditions on the final costates. Although not all of the trajectories are optimal, the computation of a single solution is very quick because no iterative procedure is implemented. Thus, the method enabled global searches for low-thrust transfers, and trade-off studies by globally filtering the optimal solutions for a wide range of time of flights. An example was shown for transfers from a near circular 125,000 km orbit at the Earth to a 50,000 km distant retrograde orbit at the Moon in the PCR3BP [for another example, see Russell (2007)].

3 Global search approach

This paper implements a global search method that is similar to that of Russell (2007), but computes low-thrust trajectory solutions from a lower Earth orbit of approximately 35827 km altitude, which requires more revolutions around the Earth, to the vicinity of the Moon with a Jacobi constant greater than that of L_1 (thus ensuring permanent capture). Moreover, we focus on longer-time-of-flight solutions. Thus, we develop techniques to reduce the search space to a computationally manageable set. The details of the method and techniques are described in the reminder of this section.

3.1 Problem formulation

In the present study, the initial conditions are those for an approximately one-day initial periodic orbit (IPO) in the PCR3BP around the Earth with a radius similar to that of GEO. The IPO is parameterized by the time-like parameter τ (Russell 2007) ($0 \le \tau \le 0.238716$ in

Table 2 Spacecraft parameters

Parameter	Non-dimensional value	Dimensional value
Initial spacecraft mass m_0	1	1500 kg
Specific impulse I_{sp}	0.0079855841	3000 s
Exhaust velocity V_e	28.7519610842	29419.95 m/s
Maximum thrust T_{max}	0.0732492483 or 0.0366246242	0.3 or 0.15 N

Table 3 Initial conditions of the initial periodic orbit

Parameter	Value
Initial positions at $\tau = 0$	$(x, y) = (0.0976435979, 0)$
Initial velocities at $\tau = 0$	$(v_x, v_y) = (0, 2.8897406004)$

non-dimensional units), with the maximum value of τ corresponding to approximately one day, which is the period of the IPO. Therefore, τ uniquely defines the position on the IPO where the spacecraft ignites the thruster for the first time.

For every trajectory presented in the present paper, the final condition is a capture around the Moon, defined by a state close to the Moon ($x_{L_1} \leq x \leq 1.15$ and $-0.15 \leq y \leq 0.15$) and a Jacobi constant higher than that of L_1 ($C_f \geq C_{L_1}$) to ensure permanent capture near the Moon. The present study investigates low-thrust transfers of two thrust levels between these boundary states. Table 2 shows the spacecraft parameters, and Table 3 summarizes the initial conditions of the IPO. The spacecraft mass m and the thrust magnitude T are non-dimensionalized by using the initial spacecraft mass m_0. Since the present paper seeks the Pareto-front of optimal solutions, we search mass-optimal solutions for different final times of up to 695.7 days.

In summary, the initial conditions are

$$
\boldsymbol{\psi} := \begin{bmatrix} \boldsymbol{r}_0 - \boldsymbol{r}_0^*(\tau) \\ \boldsymbol{v}_0 - \boldsymbol{v}_0^*(\tau) \\ m_0 - m_0^* \\ t_0 \end{bmatrix} = \boldsymbol{0}, \tag{22}
$$

where $*$ denotes the user-defined value. The final conditions are not included in $\boldsymbol{\psi}$, because we are going to disregard the associated transversality conditions. The final time is found implicitly, as the earliest time when the final conditions are met.

3.2 Set of admissible initial conditions

The admissible initial states can be easily searched, because they belong to a one-dimensional closed set parametrized by τ. The admissible initial costates are computed using the transversality conditions. We first rewrite Eq. (7) (Russell 2007; Ozimek and Howell 2010) as

$$
J = -k m_f \quad (k > 0). \tag{23}
$$

Then the transversality condition given by Eq. (19) associated with the mass:

$$
\lambda_{m_f} = -k, \tag{24}
$$
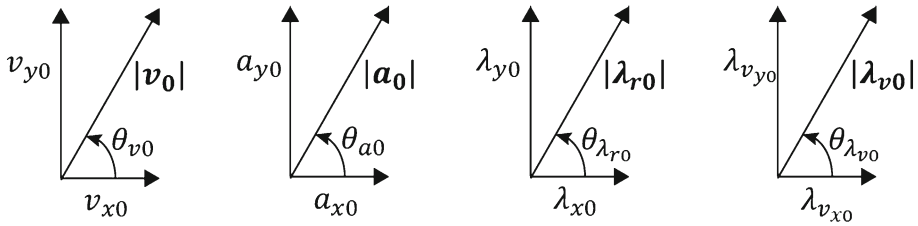
Fig. 3 Polar coordinates for the velocity, acceleration, and costates on the initial periodic orbit

is automatically satisfied by choosing

$$\lambda_{m_0} = -1, \tag{25}$$

because k is a free parameter and λ_m decreases with time. Equation (18) generates free multipliers for the initial costates, which are combined with Eq. (20) (Russell 2007)

$$\lambda_{r_0} \frac{d\boldsymbol{r}_0^*(\tau)}{d\tau} + \lambda_{v_0} \frac{d\boldsymbol{v}_0^*(\tau)}{d\tau} = 0. \tag{26}$$

The set of admissible costates is open and three dimensional, being defined by the two scalar Eqs. (25) and (26) in the five-dimensional space of $\boldsymbol{\lambda}_0$. In summary, the total set of admissible initial conditions is open and four-dimensional including τ. Though Russell (2007) globally explored the four-dimensional search set, an extensive search over this set with longer transfer times and from a lower initial orbit is computationally very costly. Therefore, we use the following techniques to reduce the search space to a manageable set.

3.3 Reduction of the search set

3.3.1 Initial thrust direction

We assume that the initial thrust direction is tangential to the IPO. Since the tangential thrust changes the Jacobi energy maximally, it could be a good option for the initial thrust direction to compute suboptimal solutions, with the advantage of reducing the search set. Thus, $\lambda_{v_{x_0}}$ and $\lambda_{v_{y_0}}$ can be related to the initial velocity v_{x_0} and v_{y_0} through Eq. (10) as

$$-\frac{\lambda_{v_{x_0}}}{|\boldsymbol{\lambda}_{v_0}|} = \frac{v_{x_0}}{|\boldsymbol{v}_0|},$$
$$-\frac{\lambda_{v_{y_0}}}{|\boldsymbol{\lambda}_{v_0}|} = \frac{v_{y_0}}{|\boldsymbol{v}_0|}. \tag{27}$$

3.3.2 Similarity to two-body dynamics

We express Eq. (26) using $\frac{d\boldsymbol{r}_0(\tau)}{d\tau} = \boldsymbol{v}_0$, $\frac{d\boldsymbol{v}_0(\tau)}{d\tau} = \boldsymbol{a}_0$ (asterisks are omitted for brevity), and the polar coordinates shown in Fig. 3 for the velocity, acceleration, and costates on the IPO as

$$|\boldsymbol{\lambda}_{r_0}||\boldsymbol{v}_0| \cos\left(\theta_{\lambda_{r_0}} - \theta_{v_0}\right) + |\boldsymbol{\lambda}_{v_0}||\boldsymbol{a}_0| \cos\left(\theta_{\lambda_{v_0}} - \theta_{a_0}\right) = 0. \tag{28}$$

Equation (27) can be rewritten as

$$\theta_{\lambda_{v_0}} = \theta_{v_0} + \pi. \tag{29}$$

Table 4 Parameters for a grid search (coarse/fine)

Parameter	Minimum	Maximum	Number of grid points
τ	0	0.238716	100
$|\boldsymbol{\lambda}_{r_0}|$	0.7	5/1	1500/2000
ϵ	-0.00014	0.00014	1500/2000

Table 5 Admissible region of trajectories

Parameter	Value	Unit
Absolute values of positions	$|x| \leq 1.2$, $|y| \leq 1.2$	–
Minimum distance from the center of the Earth	41000	km
Minimum distance from the center of the Moon	R_M	km
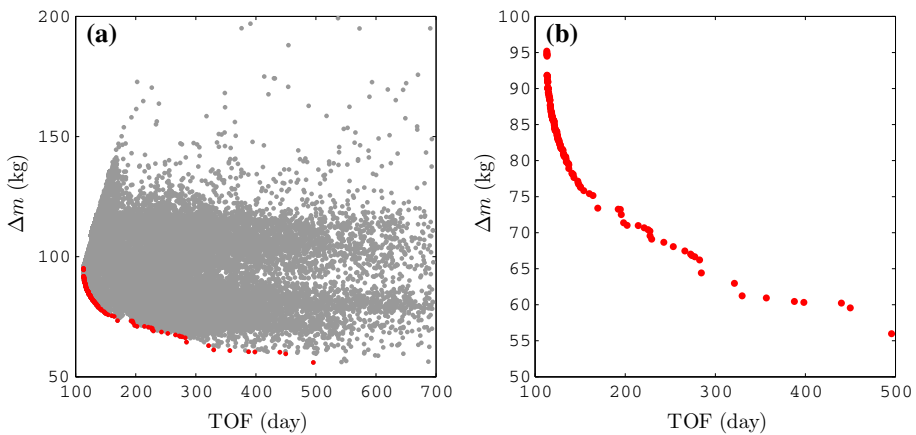
Fig. 4 **a** Pareto (*dark*) and non-Pareto (*light*) solutions in terms of time of flight (TOF) and mass consumption (Δm) for the case in which $T_{max} = 0.3$ N. **b** Pareto solutions extracted from **a**

Substituting Eq. (29) into Eq. (28) yields

$$|\boldsymbol{\lambda}_{v_0}| = \frac{|\boldsymbol{v}_0|}{|\boldsymbol{a}_0|}|\boldsymbol{\lambda}_{r_0}|\frac{\cos(\theta_{\lambda_{r_0}} - \theta_{v_0})}{\cos(\theta_{v_0} - \theta_{a_0})}, \tag{30}$$

which is used to determine $|\boldsymbol{\lambda}_{v_0}|$ as a function of $|\boldsymbol{\lambda}_{r_0}|$ and $\theta_{\lambda_{r_0}}$.

The dynamics on the IPO resembles the circular orbit in the two-body problem, and the velocity and the acceleration on the IPO are nearly perpendicular to each other:

$$\cos(\theta_{v_0} - \theta_{a_0}) \approx 0. \tag{31}$$

Thus, from Eqs. (30) and (31), we have

$$\cos(\theta_{\lambda_{r_0}} - \theta_{v_0}) \approx 0, \tag{32}$$
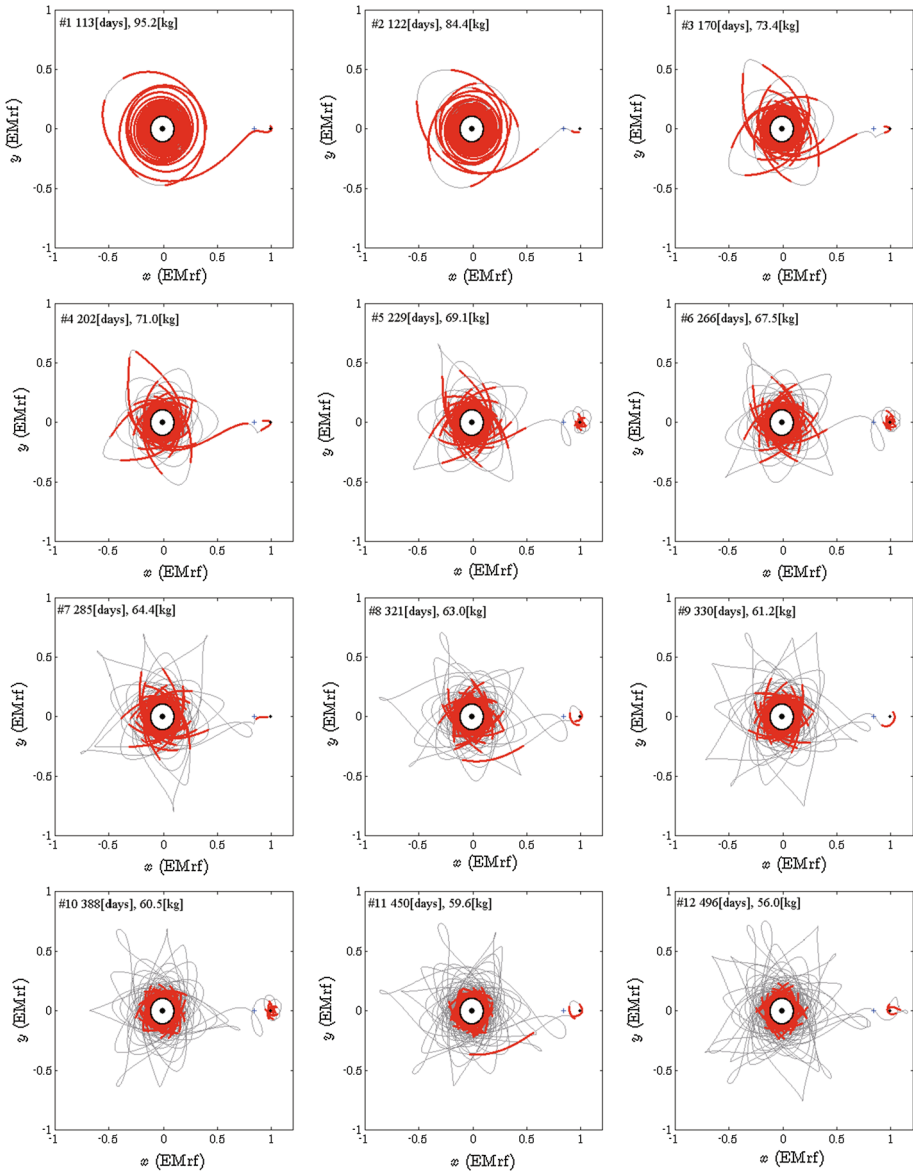
Fig. 5 Trajectories of the selected Pareto solutions shown in Fig. 4b. The nearly circular *thick* orbit represents the initial periodic orbit around the Earth. The *two black points* indicate the Earth (*left*) and the Moon (*right*), and the *numbers* indicate the TOF and Δm, respectively
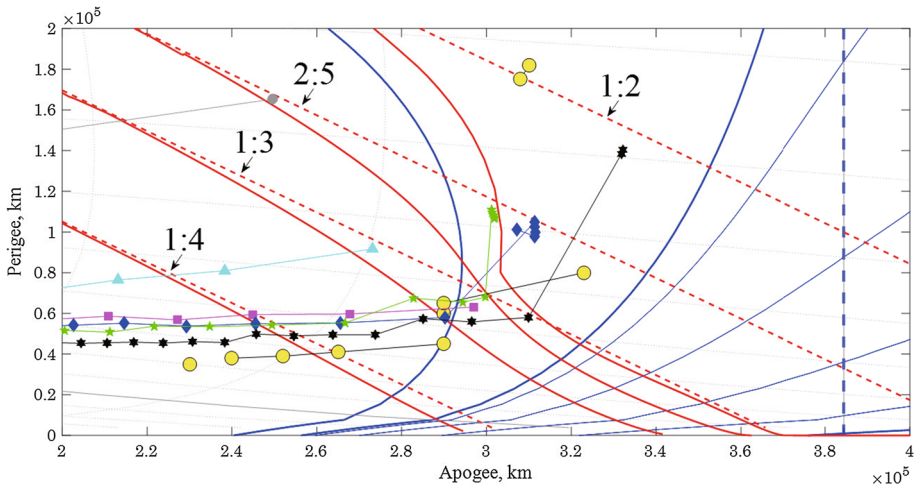
or equivalently,

$$
\begin{aligned}
\theta_{\lambda_{r_0}} - \theta_{v_0} &= \frac{\pi}{2} + \epsilon, \\
\theta_{\lambda_{r_0}} - \theta_{v_0} &= -\frac{\pi}{2} + \epsilon,
\end{aligned}
\tag{33}
$$

where $|\epsilon| \ll 1$.
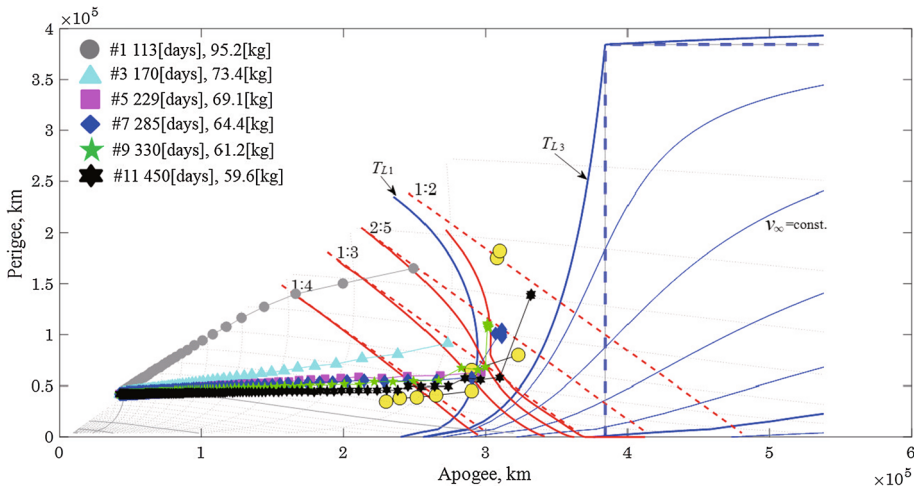
Fig. 6 Osculating perigees and apogees of the Pareto solutions of odd numbers in Fig. 5 in the T–P graph

Fig. 7 Magnification of the final part of transfers in Fig. 6

From Eq. (33), we use ϵ as a parameter to compute $\theta_{\lambda_{r_0}}$. Since the signs of both sides of Eq. (30) must be the same, we need only investigate ϵ, which satisfies

$$\frac{\cos(\theta_{\lambda_{r_0}} - \theta_{v_0})}{\cos(\theta_{v_0} - \theta_{a_0})} \geq 0. \tag{34}$$

In summary, our method requires a search over the three-dimensional $\tau - |\lambda_{r_0}| - \epsilon$ set, but with $|\epsilon| \ll 1$. Since the dimension of the search set directly affects computational cost, the presented techniques ease the global search for low-thrust transfers.

It could be possible to apply the presented techniques to other problems such as targeting a specific orbit around the Moon, where initial guesses could be provided for subsequent local optimization, and a global search from a specific near-circular, inclined initial orbit in the spatial problem, where one extra dimension would be added to the search set.
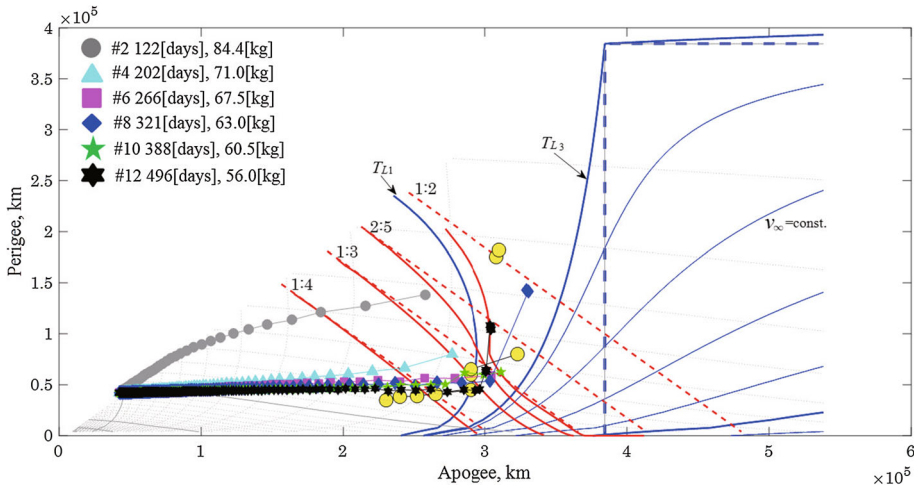
Fig. 8 Osculating perigees and apogees of the Pareto solutions of even numbers in Fig. 5 in the T–P graph
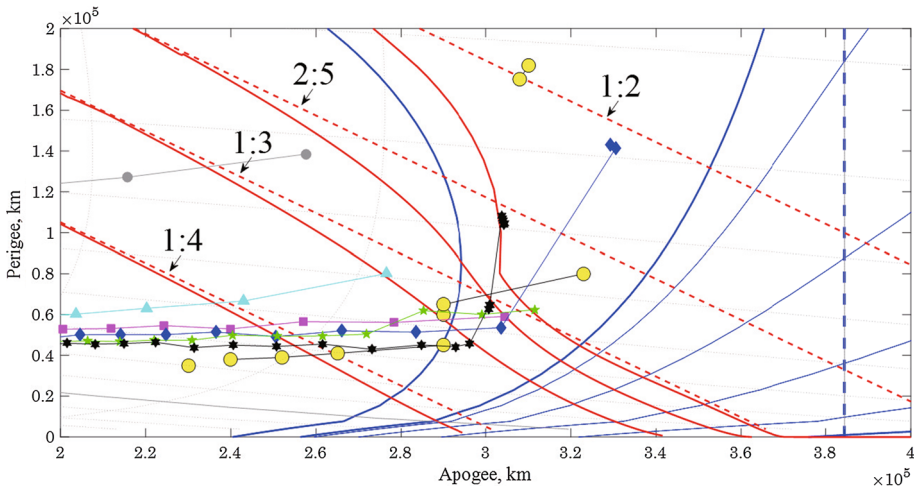

Fig. 9 Magnification of the final part of transfers in Fig. 8

4 Global search for low-thrust transfers to the Moon

Based on the procedure in the previous sections, we perform two grid searches (coarse and fine) in the $\tau - |\lambda_{r_0}| - \epsilon$ set using the Runge–Kutta–Fehlberg method of orders 4 and 5 with a tolerance of 10^{-10}. Table 4 summarizes the search set and corresponding numbers of grid points using a coarse/fine notation if needed, and Table 5 shows the admissible region of trajectories during the integration. We use all of the solutions obtained from both grid searches to show the following results.

Table 6 Final resonances of all 14 Pareto solutions with TOFs longer than 265 days for the case in which $T_{max} = 0.3$ N	Final resonance	Number of Pareto solutions
	2:5	5
	1:2	3
	1:3	6
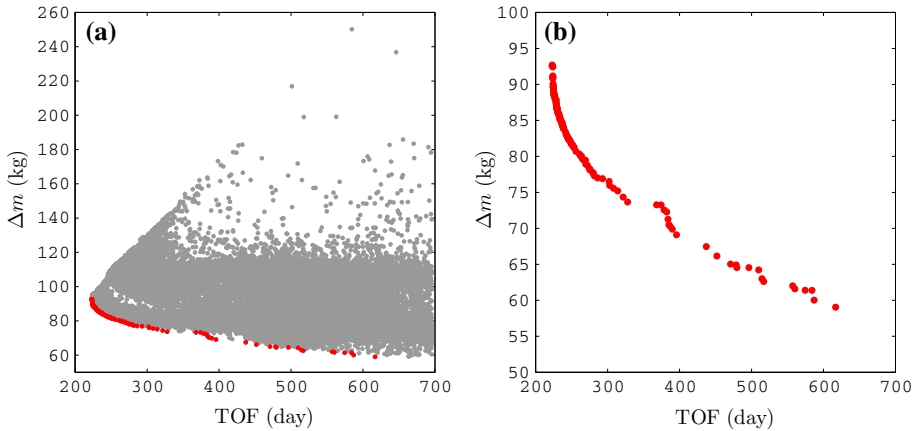
Fig. 10 **a** Pareto (*dark*) and non-Pareto (*light*) solutions in terms of TOF and Δm for the case in which $T_{max} = 0.15$ N. **b** Pareto solutions extracted from **a**

4.1 Low-thrust transfers to the Moon for $T_{max} = 0.3$ N

This section summarizes the computational results for $T_{max} = 0.3$ N and the initial mass $m_0 = 1500$ kg, which correspond to an initial acceleration that is slightly higher than that of SMART-1. Figure 4a shows the solutions in terms of time of flight (TOF) and mass consumption (Δm), where the dark points represent the Pareto solutions and the light points represent the non-Pareto solutions. For clarity, Fig. 4b shows the extracted Pareto solutions. Unfortunately, it is difficult to make a direct comparison with the results in previous works because boundary conditions are different.

Figure 5 shows the trajectories of the twelve representative Pareto solutions shown in Fig. 4b, numbered #1 to #12. The thrust arcs tend to appear near the Earth and the Moon, and the coast arcs typically appear in the "three-body" region where the lunar perturbation becomes significant.

Figures 6 and 8 show the twelve Pareto solutions on the T–P graph. For clarity, Fig. 6 shows the odd-numbered solutions and Fig. 7 shows its magnification, whereas Fig. 8 shows the even-numbered solutions and Fig. 9 shows its magnification. The T–P graph indicates that trajectories with lower perigees can exploit larger effects of resonant lunar flybys (see the boundaries of the trajectories reachable from the resonances). This is why the solutions having smaller Δm exhibit less inclined paths.

Solutions #7, #9, and #12 exploit 2:5 resonance in the final phase before reaching the Moon realm. This is in contrast to SMART-1, which used 1:2 resonance as in solutions #8 and #11. Previous studies indicated that the invariant manifolds emanating from L_1 were close to 2:5 resonance in the Earth–Moon system (Pernicka et al. 1995; Topputo et al. 2005). Thus,
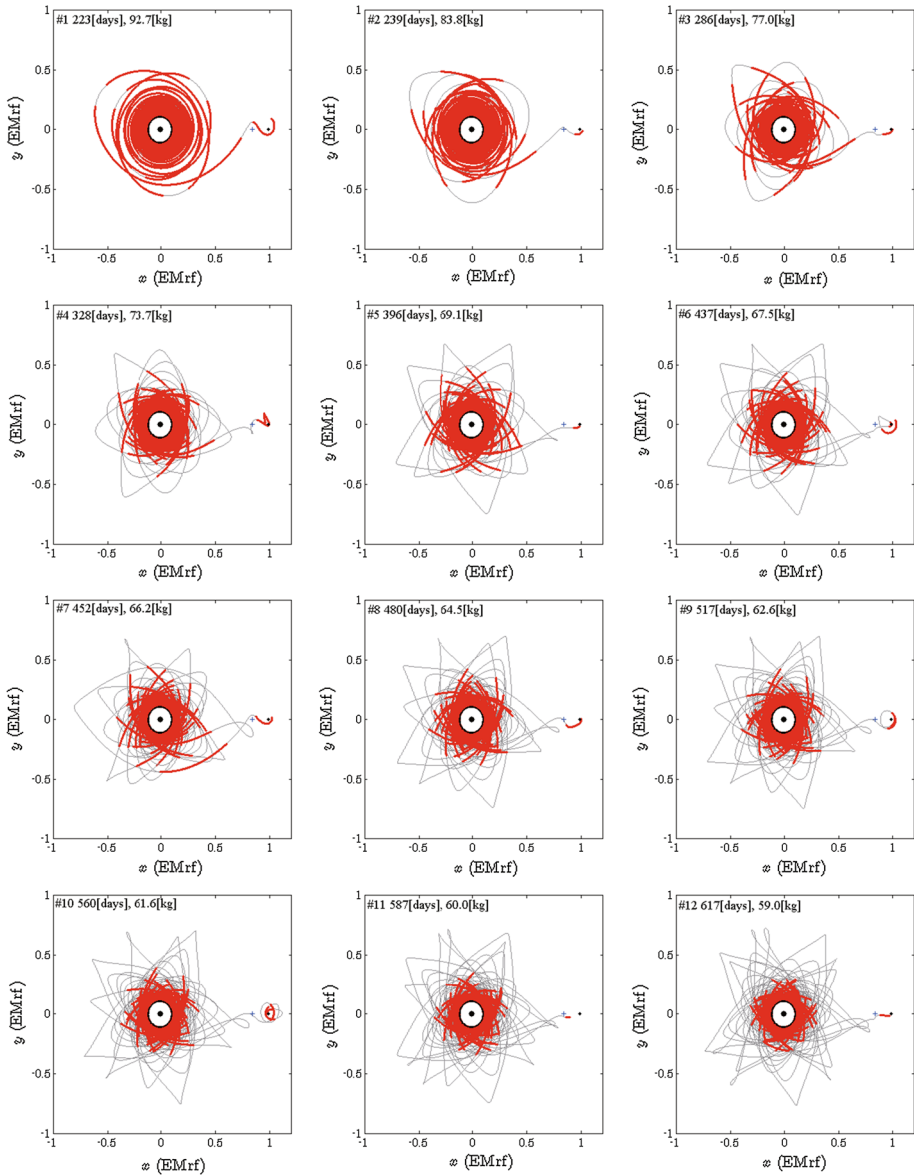
Fig. 11 Trajectories of the selected Pareto solutions from Fig. 10b. The nearly circular *thick* orbit represents the initial periodic orbit around the Earth. The *two black points* indicate the Earth (*left*) and the Moon (*right*). The *numbers* indicate the TOF and and Δm, respectively

future missions to the Moon may be able to further reduce Δm by exploiting 2:5 resonance to pass through low-energy manifold tubes (Koon et al. 2011) around L_1 while accepting some transfer time and radiation dose penalties. Table 6 summarizes the final resonances of the Pareto solutions with TOFs longer than 265 days.
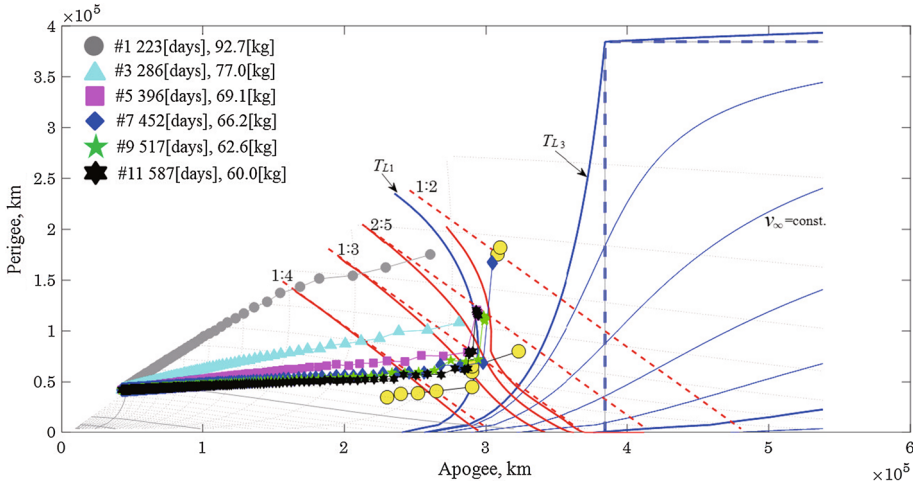
Fig. 12 Osculating perigees and apogees of the Pareto solutions of *odd* numbers in Fig. 11 in the T–P graph
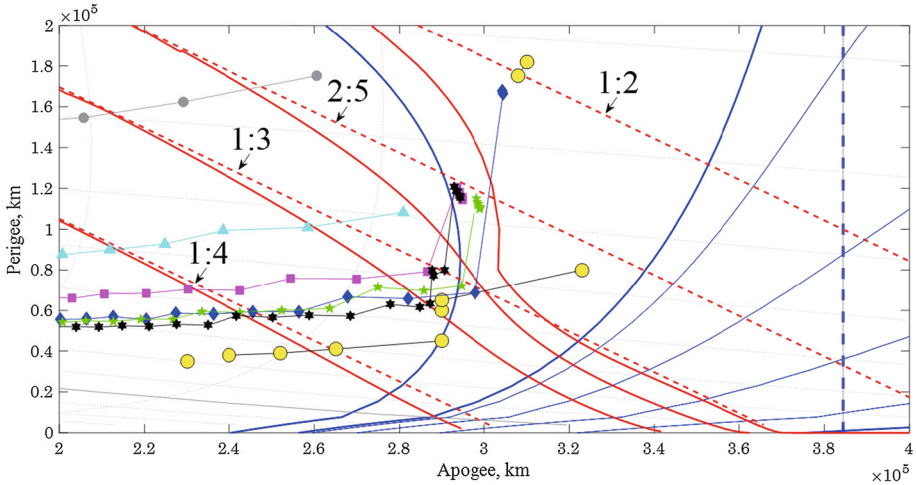
Fig. 13 Magnification of the final part of transfers in Fig. 12

## 4.2 Low-thrust transfers to the Moon for $T_{max} = 0.15$ N

This section summarizes the computational results for $T_{max} = 0.15$ N and the same initial mass, $m_0 = 1500$ kg, which correspond to an initial acceleration similar to that of the JAXA proposed DESTINY mission (Kawakatsu et al. 2014).

Figure 10a shows the solutions in terms of TOF and Δm. For clarity, Fig. 10b shows the extracted Pareto solutions. Since the acceleration is smaller than that in Sect. 4.1, the solutions have longer TOFs.

Figure 11 shows the trajectories of the twelve representative Pareto solutions in Fig. 10b, numbered from #1 to #12. Trajectories for which $T_{max} = 0.15$ N include longer intervals of thrust arcs, as compared to those for which $T_{max} = 0.3$ N, but exploit lunar flybys to reduce fuel consumption.
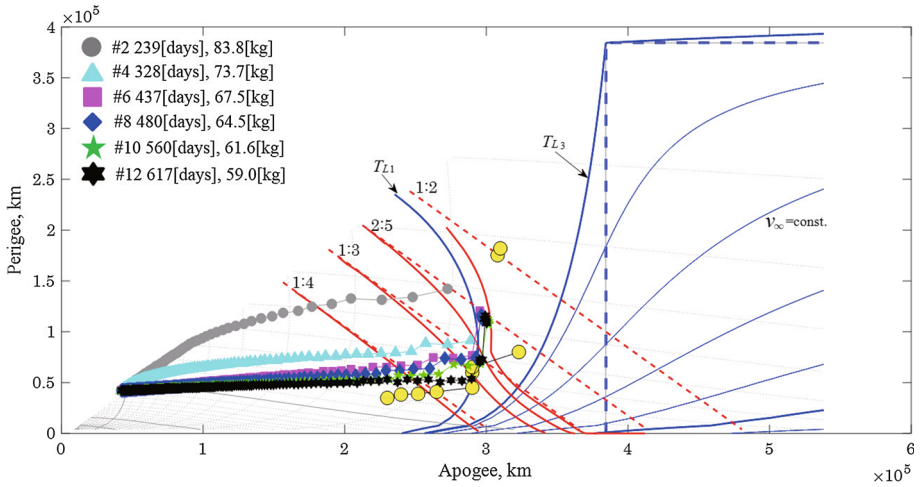
Fig. 14 Osculating perigees and apogees of the Pareto solutions of even numbers in Fig. 11 in the T–P graph
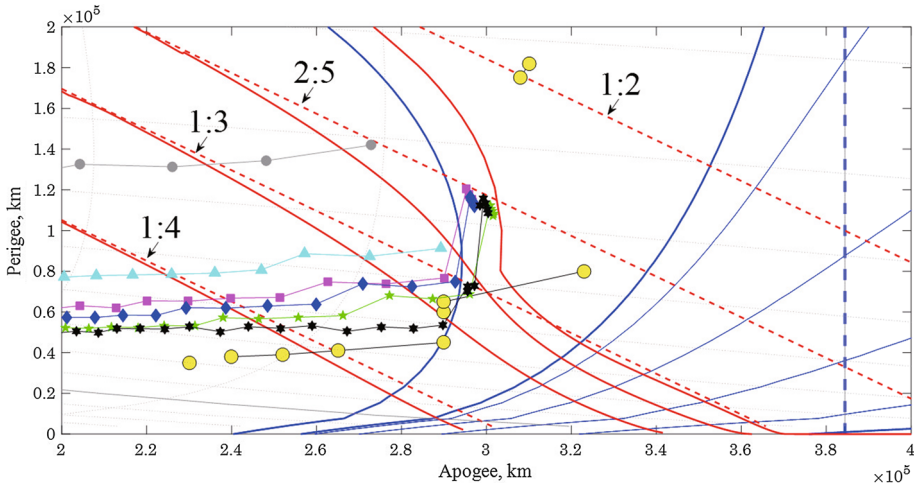

Fig. 15 Magnification of the final part of transfers in Fig. 14

Table 7 Final resonances of all 24 Pareto solutions with TOFs longer than 365 days for the case in which $T_{max} = 0.15$ N

Final resonance	Number of Pareto solutions
2:5	17
1:2	6
1:3	1

Figures 12 and 14 show the twelve Pareto solutions on the T–P graph. For clarity, Fig. 12 shows the odd-numbered solutions and Fig. 13 shows its magnification, whereas Fig. 14 shows the even-numbered solutions and Fig. 15 shows its magnification. As summarized in Table 7, many Pareto solutions with small Δm and long TOF exploit the 2:5 resonance before reaching the Moon realm.
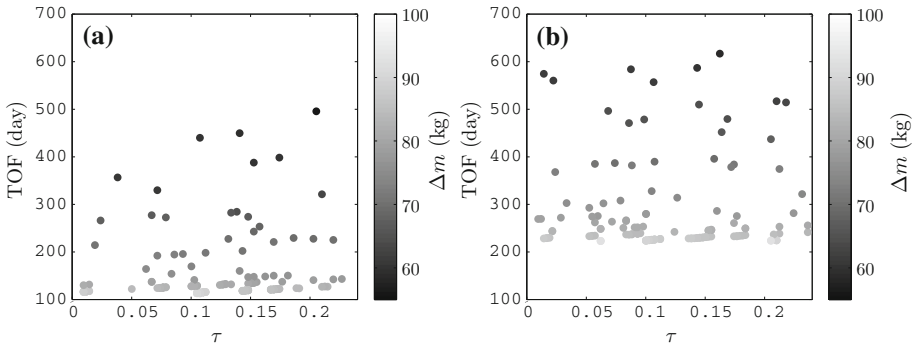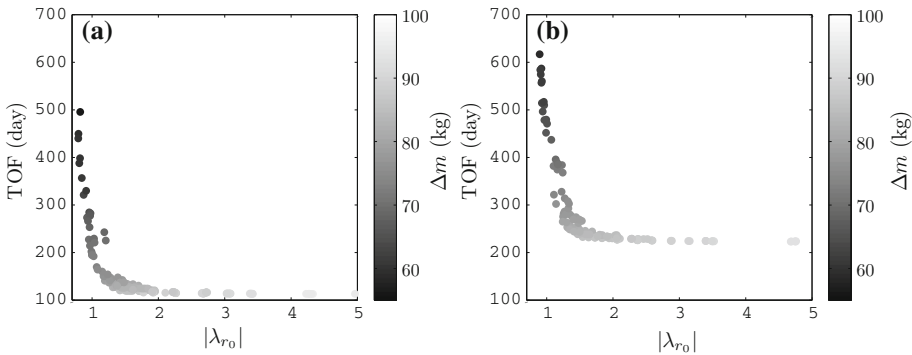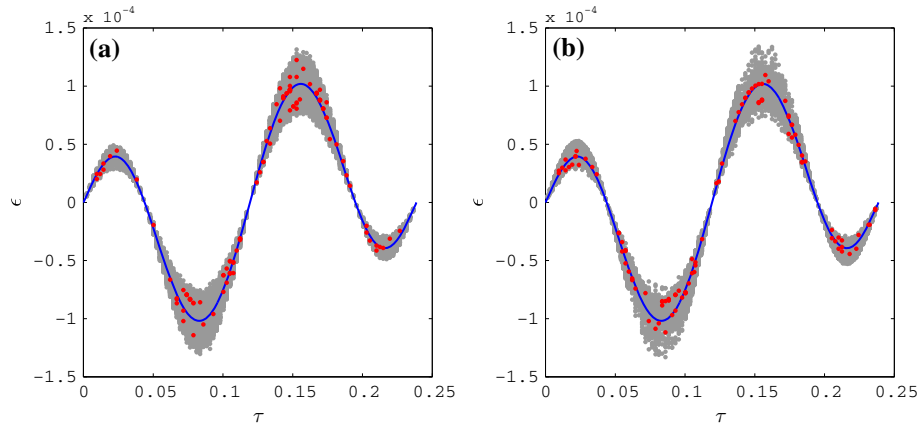
Fig. 16 Distribution of Pareto solutions for **a** $T_{max} = 0.3\,\text{N}$ and **b** $T_{max} = 0.15\,\text{N}$ in terms of TOF and the parameter τ, *shaded* in accordance with the value of Δm
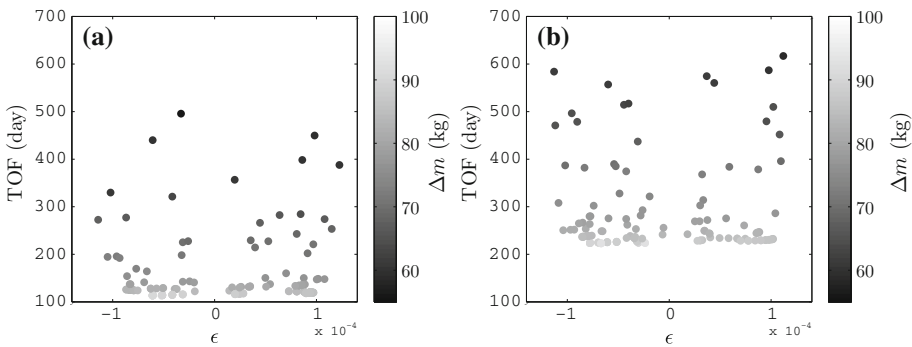
Fig. 17 Distribution of Pareto solutions for **a** $T_{max} = 0.3\,\text{N}$ and **b** $T_{max} = 0.15\,\text{N}$ in terms of TOF and the parameter ϵ, *shaded* in accordance with the value of Δm

Fig. 18 Distribution of Pareto solutions for **a** $T_{max} = 0.3\,\text{N}$ and **b** $T_{max} = 0.15\,\text{N}$ in terms of TOF and the parameter $|\lambda_{r_0}|$, *shaded* in accordance with the value of Δm

4.3 Distribution of solutions

Figure 16 shows the distribution of the Pareto solutions for (a) $T_{max} = 0.3\,\text{N}$ and (b) $T_{max} = 0.15\,\text{N}$ in terms of the TOF and the parameter τ, shaded in accordance with

Fig. 19 Distribution of Pareto (*dark dots*) and non-Pareto (*light dots*) solutions for **a** $T_{max} = 0.3$ N and **b** $T_{max} = 0.15$ N in terms of the parameters τ and ϵ. The *curve* represents ϵ' in Eq. (35)

the value of Δm. Figures 17 and 18 show the distributions of the Pareto solutions for (a) $T_{max} = 0.3$ N and (b) $T_{max} = 0.15$ N in terms of the TOF and the parameters ϵ and $|\lambda_{r_0}|$ respectively. The value of ϵ corresponds to the first equation of Eq. (33) because the second equation of Eq. (33) always violates the constraints for the minimum distance from the Earth in Table 5.

The Pareto solutions for both values for T_{max} exhibit no tendencies for τ or ϵ, but show the characteristic distributions for $|\lambda_{r_0}|$, i.e., solutions with smaller $|\lambda_{r_0}|$ tend to result in smaller Δm but longer TOF. Therefore, these results indicate that $|\lambda_{r_0}|$ characterizes the families of low-thrust transfers to the Moon. Note that Fig. 18 indicates the existence of even faster or cheaper solutions beyond the bounds on $|\lambda_{r0}|$. However, we already computed a wide range of Pareto solutions, the fastest solution of which is a nearly continuous-thrust transfer and the cheapest solution of which is a multiple-gravity-assisted transfer, and searching even faster or cheaper solutions is beyond the scope of this paper.

4.4 Further refinement for ϵ

Figure 19 shows the distribution of the Pareto (dark dots) and non-Pareto (light dots) solutions for (a) $T_{max} = 0.3$ N and (b) $T_{max} = 0.15$ N in terms of the parameters τ and ϵ. The curve represents

$$\epsilon' = -\frac{\pi}{2} + \theta_{a_0} - \theta_{v_0}, \tag{35}$$

which heuristically replaces $\theta_{\lambda_{r_0}}$ with θ_{a_0} in the first equation of Eq. (33).

Since the obtained solutions shadow the curve of ϵ', Fig. 19 indicates a heuristic that we can target ϵ in the vicinity of ϵ' in order to further reduce the search set of ϵ in future studies.

5 Conclusions

In the present paper, we presented global searches of low-thrust transfers to the Moon in the planar, circular, restricted, three-body problem. The method used herein implements the necessary conditions of optimality from the Pontryagin principle to define an initial search

space that is four dimensional and open. We assumed an initial tangential thrust and used an analogy with two-body dynamics to reduce the size of the search space. For two representative thrust levels, we computed a wide range of Pareto solutions in terms of time of flight and mass consumption, including many long-time-of-flight solutions that had not been fully explored in previous studies. Analysis via a Tisserand–Poincaré graph showed that numerous solutions exploit high-altitude lunar flybys, and 2:5 resonance is useful for reducing fuel consumption. A new heuristic indicated the possibility of further reducing the search set in future studies.

References

Abraham, A.J., Spencer, D.B., Hart, T.J.: Optimization of preliminary low-thrust trajectories from GEO-energy orbits to Earth–Moon, L_1, Lagrange point orbits using particle swarm optimization. In: AAS/AIAA Astrodynamics Specialist Conference, AAS 13-925, Hilton Head, (2013)

Betts, J.T., Erb, S.O.: Optimal low thrust trajectories to the Moon. SIAM J. Appl. Dyn. Syst. **2**, 144–170 (2003). doi:10.1137/S1111111102409080

Belbruno, E., Topputo, F., Gidea, M.: Resonance transitions associated to weak capture in the restricted three-body problem. Adv. Space. Res. **42**, 1330–1351 (2008). doi:10.1016/j.asr.2008.01.018

Caillau, J.B., Daoud, B., Gergaud, J.: Minimum fuel control of the planar circular restricted three-body problem. Celest. Mech. Dyn. Astr. **114**, 137–150 (2012). doi:10.1007/s10569-012-9443-x

Campagnola, S., Russell, R.P.: Endgame problem part 2: multi-body technique and T–P graph. J. Guid. Control Dyn. **33**, 476–486 (2010). doi:10.2514/1.44290

Campagnola, S., Skerritt, P., Russell, R.P.: Flybys in the planar, circular, restricted, three-body problem. Celest. Mech. Dyn. Astr. **113**, 343–368 (2012). doi:10.1007/s10569-012-9427-x

Campagnola, S., Boutonnet, A., Schoenmaekers, J., Grebow, D.J., Petropoulos, A.E.: Tisserand–leveraging transfer. J. Guid. Control Dyn. **37**, 1202–1210 (2014). doi:10.2514/1.62369

Folta, D.C., Bosanac, N., Cox, A., Howell, K.C.: The Lunar IceCube mission design: construction of feasible transfer trajectories with a constrained departure. AAS/AIAA Space Flight Mechanics Meeting, AAS 16-285, Napa, (2016)

Funase, R., Koizumi, H., Nakasuka, S., Kawakatsu, Y., Fukushima, Y., Tomiki, A., et al.: 50kg-class deep space exploration technology demonstration micro-spacecraft PROCYON. In: 28th Annual AIAA/USU Conference on Small Satellites, SSC14-VI-3, (2014)

Grover, P., Ross, S.D.: Designing trajectories in a planet-moon environment using the controlled Keplerian map. J. Guid. Control Dyn. **32**, 437–444 (2009). doi:10.2514/1.38320

Jerg, S., Junge, O., Ross, S.D.: Optimal capture trajectories using multiple gravity assists. Commun. Nonlinear Sci. Numer. Simul. **14**, 4168–4175 (2009). doi:10.1016/j.cnsns.2008.12.009

Kawaguchi, J., Fujiwara, A., Uesugi, T.: Hayabusa-Its technology and science accomplishment summary and Hayabusa-2. Acta Astronaut. **62**, 639–647 (2008). doi:10.1016/j.actaastro.2008.01.028

Kawakatsu, Y., et al.: DESTINY mission proposal, ISAS/JAXA Technical Note (2014)

Kluever, C.A., Pierson, B.L.: Optimal low-thrust three-dimensional Earth–Moon trajectories. J. Guid. Control Dyn. **18**, 830–837 (1995). doi:10.2514/3.21466

Koon, W.S., Lo, M.W., Marsden, J.E., Ross, S.D.: Dynamical Systems, the Three-Body Problem and Space Mission Design. Marsden Books, Wellington (2011)

Lantoine, G., Russell, R.P., Campagnola, S.: Optimization of low-energy resonant hopping transfers between planetary moons. Acta Astronaut. **68**, 1361–1378 (2011). doi:10.1016/j.actaastro.2010.09.021

Lawden, D.F.: Optimal Trajectories for Space Navigation. Butterworths, London (1963)

Mingotti, G., Topputo, F., Bernelli-Zazzera, F.: Low-energy, low-thrust transfers to the Moon. Celest. Mech. Dyn. Astr. **105**, 61–74 (2009). doi:10.1007/s10569-009-9220-7

Ohndorf, A., Bachwald, B., Gill, E.: Optimization of low-thrust Earth–Moon transfers using evolutionary neurocontrol. In: IEEE Congress on Evolutionary Computation, Trondheim, (2009)

Ozimek, M.T., Howell, K.C.: Low-thrust transfers in the Earth–Moon system, including applications to libration point orbits. J. Guid. Control Dyn. **33**, 533–549 (2010). doi:10.2514/1.43179

Pernicka, H.J., Scarberry, D.P., Marsh, S.M., Sweetser, T.H.: A search for low Δv Earth-to-Moon trajectories. J. Astronaut. Sci. **43**, 77–88 (1995)

Pontryagin, L.S.: Mathematical Theory of Optimal Processes. CRC Press, Boca Raton (1987)

Racca, G.D., Marini, A., Stagnaro, L., van Dooren, J., di Napoli, L., Foing, B.H., et al.: SMART-1 mission description and development status. Planet. Space Sci. **50**, 1323–1337 (2002). doi:10.1016/S0032-0633(02)00123-X

Rayman, M.D., Varghese, P., Lehman, D.H., Livesay, L.L.: Results from the deep space 1 technology validation mission. Acta Astronaut. **47**, 475–487 (2000). doi:10.1016/S0094-5765(00)00087-4

Ross, S.D., Lo, M.W.: Design of a multi-moon orbiter. In: AAS/AIAA Space Flight Mechanics Meeting, AAS 03-143, Puerto Rico, (2003)

Ross, S.D., Scheeres, D.J.: Multiple gravity assists, capture, and escape in the restricted three-body problem. SIAM J. Appl. Dyn. Syst. **6**, 576–596 (2007). doi:10.1137/060663374

Russell, R.P.: Primer vector theory applied to global low-thrust trade studies. J. Guid. Control Dyn. **30**, 460–472 (2007). doi:10.2514/1.22984

Russell, C.T., Barucci, M.A., Binzel, R.P., Capria, M.T., Christensen, U., Coradini, A., et al.: Explore the asteroid belt with ion propulsion: dawn mission history, status and plans. Adv. Space. Res. **40**, 193–201 (2007). doi:10.1016/j.asr.2007.05.083

Szebehely, V.: Theory of Orbits: The Restricted Problem of Three Bodies. Academic Press Inc, New York (1967)

Topputo, F.: Low-thrust non-Keplerian orbits: analysis, design, and control. Disseartation, Politecnico di Miano (2007)

Topputo, F., Vasile, M., Bernelli-Zazzera, F.: Earth-to-Moon low energy transfers targeting L_1 hyperbolic transit orbits. Ann. N.Y. Acad. Sci. **1065**, 55–76 (2005). doi:10.1196/annals.1370.025

Topputo, F., Belbruno, E., Gidea, M.: Resonant motion, ballistic escape, and their applications in astrodynamics. Adv. Space. Res. **42**, 1318–1329 (2008). doi:10.1016/j.asr.2008.01.017

Zhang, C., Topputo, F., Bernelli-Zazzera, F., Zhao, Y.: Low-thrust minimum-fuel optimization in the circular restricted three-body problem. J. Guid. Control Dyn. **38**, 1501–1510 (2015). doi:10.2514/1.G001080